



Original Article

Transparent magnesium aluminate spinel: Effect of critical temperature in two-stage spark plasma sintering

A. Talimian^{a,*}, V. Pouchly^{b,c}, H.F. El-Maghraby^{a,d,e}, K. Maca^{b,c}, D. Galusek^{a,d}^a Centre for Functional and Surface Functionalised Glass, Alexander Dubcek University of Trencin, Trencin, Slovakia^b CEITEC BUT, Brno University of Technology, Purkynova 123, Brno, Czech Republic^c Faculty of Mechanical Engineering, Brno University of Technology, Technicka 2, Brno, Czech Republic^d Joint Glass Centre of the IIC SAS, TnUAD and FChPT STU, Trencin, Slovakia^e Refractories, Ceramics, and Building Materials Department, National Research Centre, 33 El-Bohous St., 12622, Cairo, Egypt

ARTICLE INFO

Keywords:

Magnesium aluminate spinel
Spark plasma sintering
Carbon contamination
Optical properties

ABSTRACT

The discolouration of magnesium aluminate spinel caused by carbon contamination is a main drawback of fabricating transparent bodies by spark plasma sintering (SPS). In this study, a two-stage heating rate profile was used to produce transparent MgAl_2O_4 without using sintering aids by SPS at 1250°C. The effect of critical temperature (T_c), at which the heating rate is decreased, on transparency and carbon contamination was investigated: higher critical temperature resulted in higher contamination. Non-uniform densification indicated that fast heating results in a hot-zone formation in the centre of sintered pellets; the higher temperature of centre favoured reaction of graphite die with spinel and formation of disordered carbon structures in residual pores.

1. Introduction

Magnesium aluminate spinel is a promising optical ceramics due to its high transparency over a wide window of electromagnetic radiation, from ultraviolet to mid-infrared (0.2–5.5 μm). Its crystal structure is capable of hosting a variety of optically active ions and, hence, the optical properties can be modified [1–4]. Having an optically isotropic structure, highly transparent bodies are obtained by producing highly dense green bodies and removing the pores, acting as light scattering centres, by a suitable sintering process [5–9]. Fabricating a highly dense magnesium aluminate spinel is, however, a difficult task. Due to slow diffusion of atomic species, particularly oxygen, transparent magnesium aluminate spinel is usually fabricated either in two steps by pressure-less sintering followed by hot isostatic pressing or a lengthy hot pressing process (HP) [10–13]. Subjecting magnesium aluminate spinel to high temperatures for a long time results in grain growth, changes the microstructure and deteriorates mechanical properties [13–16].

Spark plasma sintering (SPS) is a practical method of fabricating highly dense fine-grained ceramics. However, the carbon contamination of materials prepared by SPS is inevitable [17–23]. Addition of lithium fluoride facilitates densification of spinel ceramics and cleanses the carbon contamination. However, the interactions between LiF and MgAl_2O_4 yield detrimental phases, introduce structural defects (i.e. F

centres) and deteriorate optical properties of the final body [21,24–27]. Carbon contamination can be also minimised by optimising the spark plasma sintering parameters. Several attempts have been made to study the carbon contamination and to fabricate transparent spinel without sintering aids [20,28,29]. Morita et al. have reported that the level of carbon contamination is sensitive to the heating rate during SPS: slow heating improves the transparency of MgAl_2O_4 [30]. While slow heating is beneficial to transparency, it extends the duration of the process and thereby eliminates one of the main advantages of SPS, i.e. fast sintering.

In the present study, the fabrication time of transparent magnesium aluminate spinel is reduced by performing a two-stage spark plasma sintering schedule comprising of initial fast heating followed by slow heating. The effect of critical temperature, at which the heating rate is changed, on transparency and carbon contamination was investigated using a Raman spectroscopy and described following thermodynamic approach.

2. Experimental procedures

Commercial magnesium aluminate spinel powder, S30CR (Baikowski, France), was used as the starting material. The powder was dispersed in isopropanol using an ultrasonic mixer (Sonopuls HD 3400, BANDELIN, Germany). Afterwards, the mixture was transferred to a

* Corresponding author.

E-mail address: ali.talimian@tuni.sk (A. Talimian).<https://doi.org/10.1016/j.jeurceramsoc.2020.02.012>

Received 15 October 2019; Received in revised form 4 February 2020; Accepted 5 February 2020

Available online 06 February 2020

0955-2219/© 2020 The Authors. Published by Elsevier Ltd. This is an open access article under the CC BY-NC-ND license

<http://creativecommons.org/licenses/by-nc-nd/4.0/>.

rotary evaporator and the liquid removed; Ready-to-Press (RTP) powder was prepared by passing the dried powder through a sieve with 0.5 mm mesh width.

The samples were fabricated by spark plasma sintering (SPS) (DR. SINTER SPS-625, FUJI, Japan). The granulated powder was filled in a graphite die with an inner diameter of 12 mm. Graphite paper was used to separate the powder from the die and the punches. Then, the die was wrapped in carbon felt insulator. Sintering was performed under vacuum (5–9 Pa). The temperature was measured using an optical pyrometer focused on the hole drilled into a die wall. A constant uniaxial pressure of 75 MPa was applied above 800 °C.

Preliminary information on the densification behaviour of mixed spinel powder was obtained by performing a single-stage SPS. The experiments were performed by increasing the temperature of samples to 600 °C in 3 min; then, the samples were heated at 100 °C min⁻¹ to 1300 °C. Afterwards, the two-stage SPS was carried out by increasing the temperature to 600 °C in 3 min and, afterwards, the samples were heated to a temperature between 1100 °C–1200 °C with the constant heating rate of 100 °C.min⁻¹. Then, the heating rate was decreased to 2.5 °C.min⁻¹ and heating continued up to 1250 °C. The variations of temperature and applied pressure against time during sintering profiles are shown in Fig. 1.

Sintered pellets were subsequently heat treated in a muffle furnace at 800 °C (heating rate: 2.5 °C min⁻¹) for 60 min in air in order to remove residual carbon from the surfaces. The samples were carefully mirror polished on both sides using diamond abrasive papers down to 0.5 µm for further optical characterisation. The final thickness of the samples after polishing was ~1 mm.

The density of sintered bodies was measured using Archimedes' method in deionised water.

The In-line transmission was measured in the wavelength range between 200–2000 nm using a UV-vis-NIR spectrophotometer (Cary 5000, Agilent, USA) with grating and slit change at 800 nm.

Raman spectroscopy was conducted on the surface and the polished cross-section of sintered samples by using a Raman microscope spectrometer (inVia Qontor, Renishaw, UK) using 532 nm excitation wavelength at room temperature.

The microstructure was examined using scanning electron microscopy (JSM-7600 F, JEOL, Japan). The cross-section of samples was mirror-polished using 1 µm diamond paste. The fracture surfaces and polished cross-sections were thermally etched at 1150 °C for 30 min. The etched samples were fixed at aluminium sample holders using the conductive adhesive tape and, afterwards, coated with carbon; the grain size was determined from the SEM images using linear

intersection method.

3. Results

Fig. 2 shows the punch displacement (normalised by weight of samples) and the displacement rate as a function of temperature during single-stage SPS of magnesium aluminate spinel at the constant heating rate of 100 °C min⁻¹. The pressure applied by the punches plotted against sintering temperature is also shown. The displacement of punches consists of three main regions: the first stage between 800–950 °C where the shrinkage is the fastest, and the main peak in the shrinkage rate is observed. The shrinkage is attributed to application of pressure at 800 °C resulting in particle rearrangement. This is followed by a continuous shrinkage, with a constant rate between 950–1100 °C. Finally, the densification slows down, and the shrinkage rate decreases significantly. The shrinkage eventually stops above 1250 °C where the displacement curve reaches a plateau, and a density of > 99.0 % is achieved. Therefore, the maximum sintering temperature was limited to 1250 °C to eliminate phenomena such as grain growth and pore coalescence.

A set of various sintering regimes was applied: the heating rate was decreased to 2.5 °C.min⁻¹ after a specific temperature in the interval between 1100–1200 °C (namely 1100, 1150, 1175 and 1200 °C) was achieved. In the latter text, this temperature is denoted as critical temperature, T_c . Fig. 3 shows the appearance, and the values of in-line transmissions measured at 550 nm of samples produced by SPS, using different T_c between 1100 °C–1200 °C. A sample produced by slow heating from 1100 °C to 1200 °C is also shown. Samples produced with the $T_c = 1100$ and 1150 °C are almost transparent and exhibit a maximum transmission of 65 and 67 %. The sample fabricated using $T_c = 1175$ °C has a large dark spot in the centre, and the transmission decreases to 51 %. The sample sintered with a T_c of 1200 °C is almost entirely black with a limited transmission of 10 %. However, the periphery of the pellet is transparent. The sample sintered by slow heating from 1100–1200 °C, is transparent in the centre, but it is opaque and whitish at the edges, indicating the presence of large pores and incomplete sintering.

Fig. 4 shows the in-line transmission, ILT, of the samples as a function of the incident light wavelength measured in the range between 200–2000 nm. The measured ILT is recalculated to the same thickness of $d_2 = 1.0$ mm, using Eq. 1[16]:

$$ILT(d_2) = (1 - R_s)^2 \left(\frac{ILT(d_1)}{1 - R_s} \right)^{\frac{d_2}{d_1}} \quad (1)$$

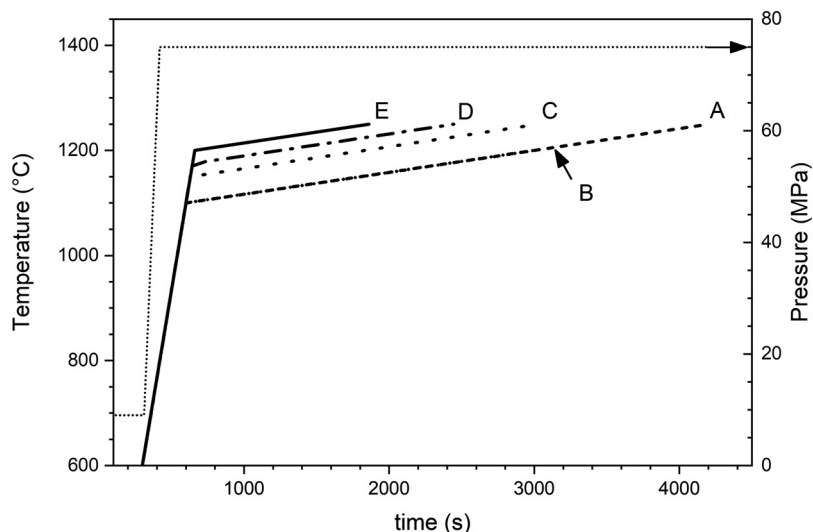


Fig. 1. Temperature and pressure against time of two-stage spark plasma sintering profiles.

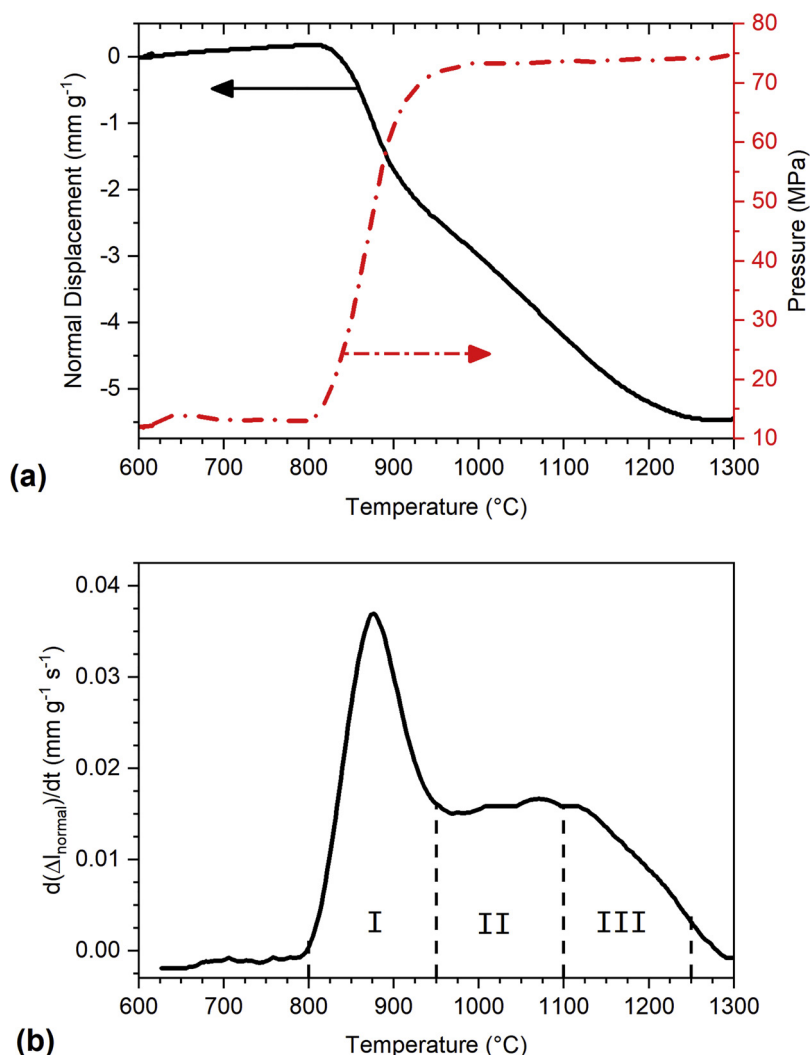


Fig. 2. (a) Punch displacement (normalised by weight) and pressure against temperature as a function of temperature; (b) first derivative of punch displacement.

where R_S is the total surface reflectance (≈ 0.14), and $ILT(d_t)$ is the value obtained for the sample with the thickness d_t . A discontinuity at the ILT curve that is observed at 800 nm, and recorded for all samples, is related to instrumental limitations and the detector and grating change-over. Therefore, the measured spectrum is divided into two regions: 200–795 nm, and 805–2000 nm. Samples produced using T_c of 1100 and 1150 °C exhibit similar transmission in both IR and UV ranges with a sharp decrease in transmission at $\lambda = 300$ nm. Conversely, the transmission of samples produced with a $T_c = 1175$ °C, decreases with a shallow slope as the wavelength decreases. The blackening of transparent bodies fabricated by spark plasma sintering is attributed to carbon contamination [29–31].

The distribution of carbon in samples was examined by Raman spectroscopy. Fig. 5 shows micro-Raman spectra collected over the surface of samples fabricated using a sintering regime with the critical temperature of 1150 °C (the highest transparency) and 1200 °C (the lowest transparency); Raman spectra of the used carbon paper and RTP spinel powder are also shown.

The Raman spectrum of the as-received powder contains five major peaks attributed to vibration modes of magnesium aluminate spinel and three other peaks corresponding to sulphate, chloride and carbonate species. The strong peaks located around 410, 672 and 770 cm^{-1} are associated with E_g , T_{2g} and A_{1g} vibrations of MgAl_2O_4 , respectively. The weak band centred around 311 cm^{-1} is attributed to T_{2g} vibration of MgAl_2O_4 . The peak located at 727 cm^{-1} is associated with the breathing

mode of aluminium cations located in tetrahedral sites implying that inverse spinel structure exists in the powder [5,32–35]. The peak around 980 cm^{-1} is attributed to the vibration of SO_x species. There are also two more peaks assigned to the vibration modes of trace Cl_2 and CO_3^{2-} at 560 and 1064 cm^{-1} , respectively [36]. The chloride, sulphate and carbonate species originate from the process of powder synthesis [37].

The peaks of impurities at 560, 980 and 1064 cm^{-1} disappeared entirely in the samples subjected to spark plasma sintering. Instead, the Raman spectrum of the sample produced at the $T_c = 1200$ °C is distinctively different from the spectrum of the sample fabricated at the $T_c = 1150$ °C: it exhibits a strong peak associated with the D-band mode of disordered graphite (1350 cm^{-1}). In contrast, the Raman spectrum of carbon paper exhibits a strong peak at around 1580 cm^{-1} that is associated with the G-band mode of graphite and a highly ordered structure. The presence of carbon in the sintered bodies with a different structure from the carbon paper rules out the possibility that the observed blackening of samples is caused by carbon inclusions introduced from the debris of the die or carbon paper. Blackening of samples can be thus attributed to deposition of carbon formed through the reaction of carbon from graphite paper/die with MgAl_2O_4 at high temperatures.

Fig. 6 shows the Raman spectra collected near the centre of the pellets and close to the edge of the pellets' cross-sections. The spectra collected at the centre and the edge of the samples prepared at the $T_c = 1100$ °C are basically the same, implying that carbon contamination is

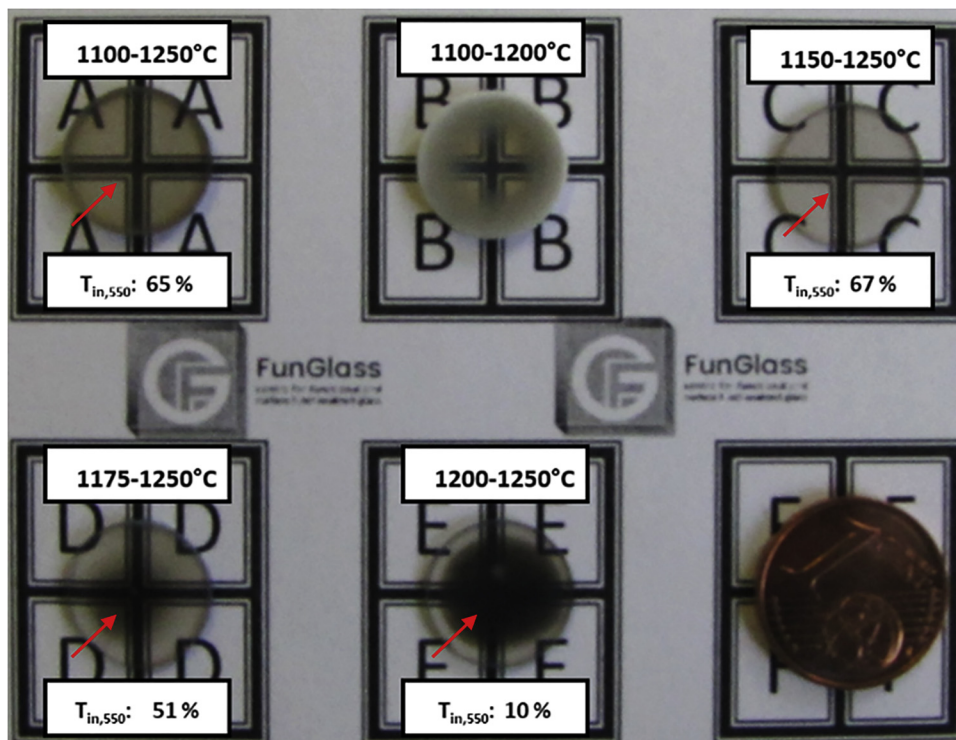


Fig. 3. Optical photographs of samples produced with the use of a slow heating regime (2.5 °C/min) between T_c and 1250 °C; the samples have a thickness of ca 1 mm and are placed directly at the background. The values of ILT were measured at a wavelength of 550 nm. (arrows point out the spot of transmission measurements (Fig. 4) and collecting Raman spectra ((Fig. 5)).

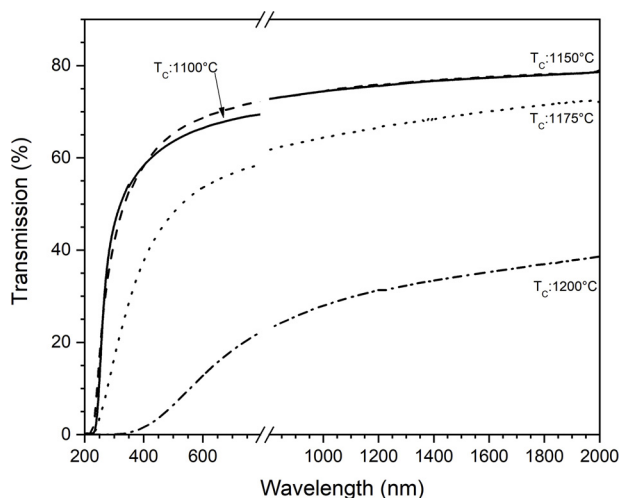


Fig. 4. In-line transmittance against the wavelength of samples fabricated by two-stage spark plasma sintering using different critical temperatures T_c : 1100, 1150, 1175 and 1200 °C. The transmission was evaluated for a thickness of 1 mm using Eq. 2.

very limited. In contrast, the peaks associated with carbon D-band (1350 cm^{-1}) and G-band (1600 cm^{-1}) start to be visible in the spectrum collected in the centre of the samples fabricated at the $T_c = 1150\text{ °C}$. The intensities of peaks associated with carbon increased significantly in the sample sintered using the $T_c = 1175\text{ °C}$. Carbon-related peaks have become the main peaks for the samples produced at the $T_c = 1200\text{ °C}$. The Raman spectra collected near the edge are essentially similar for all samples, and no peaks associated with carbon appear in the spectra. However, low-intensity peaks associated with the carbon D-band and G-band are observed in the spectrum of the sample prepared with a critical temperature of 1200 °C.

4. Discussion

4.1. Densification

The densification curve shown in Fig. 2 consists of three main steps: the first step corresponds to the powder compaction, crushing of granules and/or particle rearrangement, which appears as a fast displacement of the punch after the pressure is applied at $T = 800\text{ °C}$. The displacement rate is almost constant in the next temperature interval between 900–1100 °C. The starting temperature of this step is similar to the densification threshold for conventional sintering of the used spinel powder (S30CR, Baikowski) [38,39].

The densification produces a solid body containing isolated closed pores. The deformation of the solid body subjected to the pressure is limited and, hence, the punch displacement during the final stage of sintering ($> 1100\text{ °C}$) is caused only by sintering. At the same time, the gas pressure increases inside the closed pores, which shrink as the result of applied temperature and pressure. The increase of internal pressure of gasses also results in the decrease of shrinkage rate.

In addition to conventional sintering mechanism, i.e. grain boundary diffusion or lattice diffusion, densification during spark plasma sintering is a result of ceramics' creep under large compressive stresses [40]. Increasing concentration of lattice defects such as vacancies and dislocations introduces light scattering centres and deteriorates the transparency of ceramics [28]. However, the slip systems of magnesium aluminate spinel are not activated below 1300 °C [41,42]. Granger et al. studied the sintering behaviour of magnesium aluminate spinel during SPS and concluded that grain boundaries sliding, accommodated by the in-series reaction of interfaces and lattice diffusion of oxygen, governs the densification process [41]. Therefore, the transparency of samples is unlikely to be affected by the changes in dislocation density at the temperatures applied in this study.

Fig. 7 visualises a sample fabricated by fast heating (100 °C min^{-1}) to $T_c = 1100\text{ °C}$ followed by slow heating (2.5 °C min^{-1}) to 1200 °C. While the central region of the sample is transparent (a transparent region ca. 6 mm in diameter is present), the edge of the sample is opaque. This indicates that during the sintering the samples have been

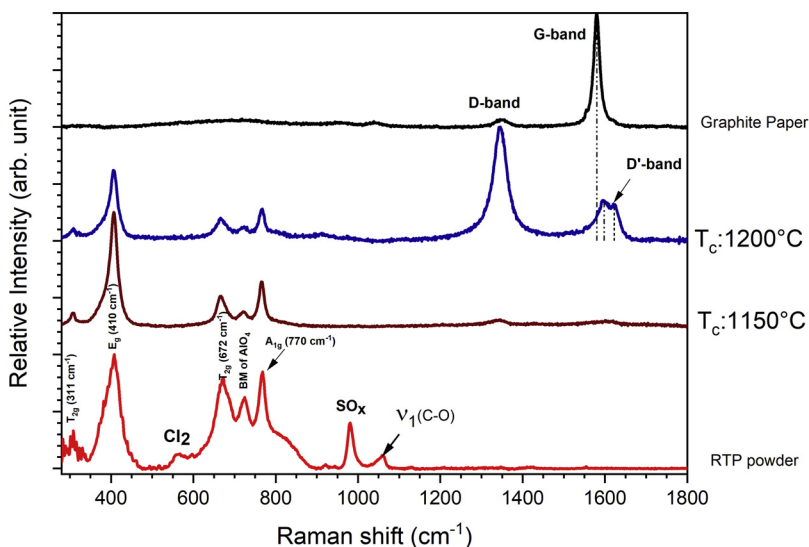


Fig. 5. Raman spectra collected from the as-received spinel powder (red line), and the samples produced by spark plasma sintering at 1250 °C using critical temperatures of 1150 °C and 1200 °C. The spectra collected from graphite paper used in SPS is shown for comparison. (For interpretation of the references to colour in this figure legend, the reader is referred to the web version of this article).

densified in-homogenously: the centre is denser than the rim and free from large pores.

Fig. 8 shows the grain size distribution in the centre and at the periphery of samples sintered at various T_c . While the grain size of samples is independent of T_c , the centre of all samples is characterised by larger grains than the peripheries. Similarly, such non-uniform distribution of grain size in ceramic bodies, e.g. Al_2O_3 and Y_2O_3 , has been reported in other works [43,44]. Three factors can be held responsible for larger grains in the centre: lower carbon contamination, a higher

concentration of defects, and temperature gradient. As shown in Fig. 3, sintered samples exhibit larger amounts of carbon in the central area. Thus carbon contamination cannot explain the non-uniform distribution of grain size. The accumulation of defects, i.e. vacancies, might be responsible for the grain growth; however, it eventually results in the increase of samples' porosity, particularly in the centre. In contrast, samples show a different distribution of pores. Fig. 9 shows the fracture surface of pellets sintered at $T_c = 1100$ °C. All observed pores are isolated and located at the grain boundaries. Moreover, the edge of the

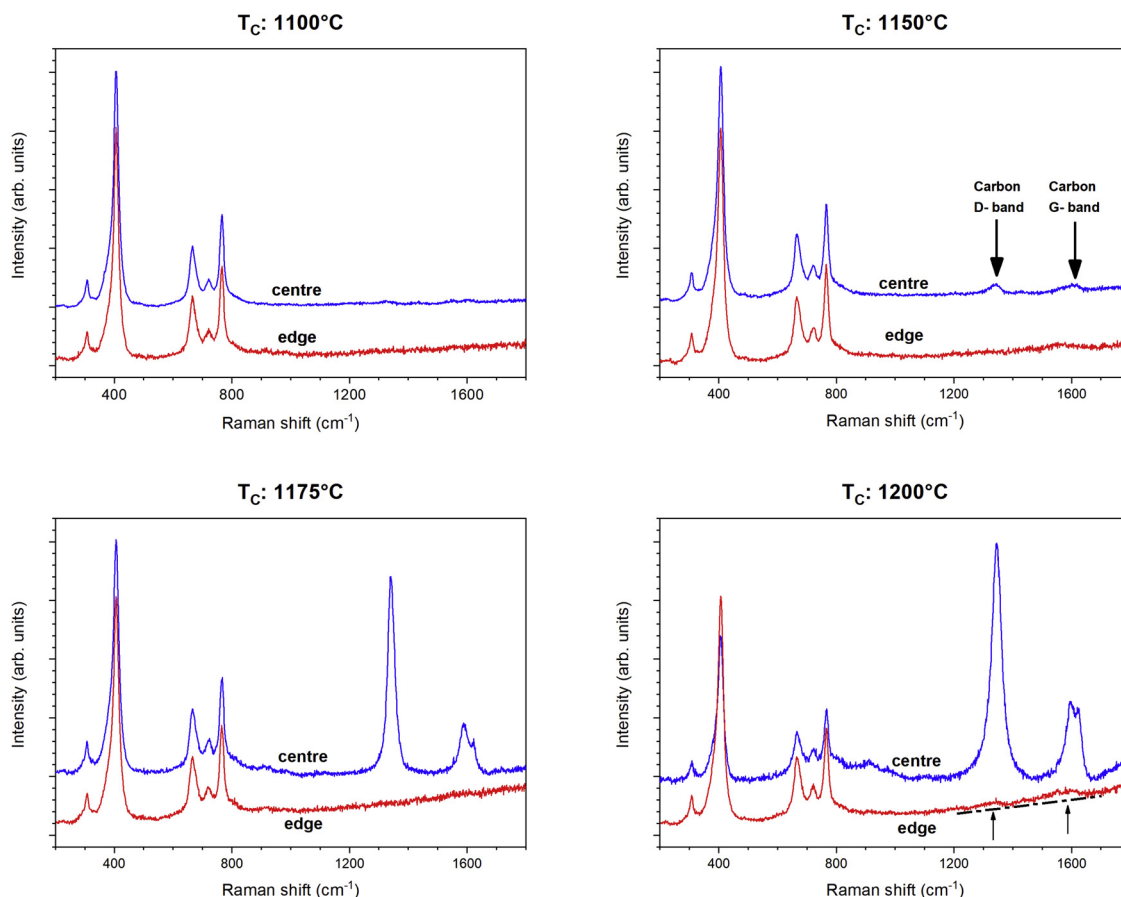


Fig. 6. Raman spectra collected from polished cross-section of samples at the edges and in the centre of samples SPSed at 1250 °C using the critical temperature of: (a) 1100 °C, (b) 1150 °C, (c) 1175 °C and (d) 1200 °C.

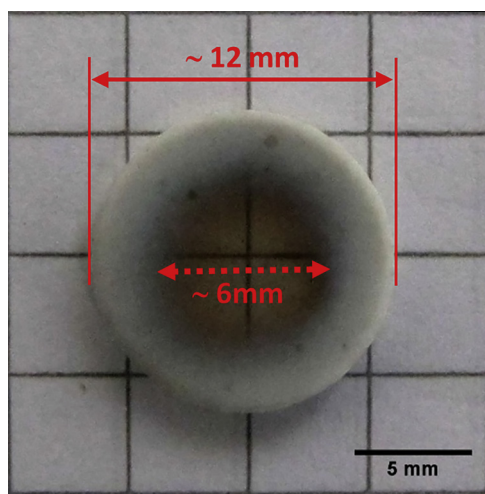


Fig. 7. Optical photographs of a spinel disk produced two-stage SPS: initial fast heating ($100\text{ }^{\circ}\text{C min}^{-1}$) to $T_c = 1100\text{ }^{\circ}\text{C}$, followed by slow heating ($2.5\text{ }^{\circ}\text{C min}^{-1}$) to $1200\text{ }^{\circ}\text{C}$.

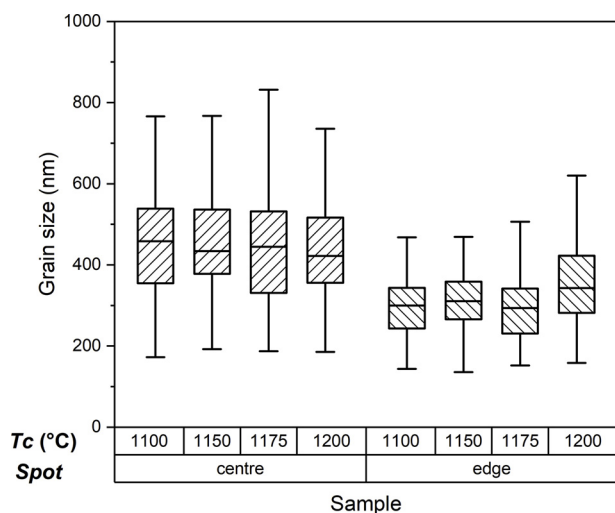


Fig. 8. Grain size distribution of samples as a function of T_c in the centre and at the edge of sintered pellets; median values, 25th and 75th percentiles, as well as maximum and minimum values are shown.

pellet contains more pores than the centre (Fig. 9a vs Fig. 9b) due to inhomogeneous densification (compare to Fig. 7) and expressed in increased opacity of the sample edge. Therefore, the increasing porosity in the periphery cannot be explained by the increase of defect concentration only.

The non-uniform densification of electrically non-conductive

materials is mainly attributed to the temperature gradient during SPS, i.e. to the third proposed mechanism [45,46]. Ceramic compacts are heated up by passing an electric current through the graphite die. Consequently, one expects that the edge of non-conductive samples is hotter than the centre. Astonishingly, the visual examination of samples prepared in this study suggests the opposite behaviour (Fig. 7). Cola-suonno reported on the inhomogeneous temperature distribution and the formation of local hot-zones in ceramics due to the electric current flow paths shift during spark plasma sintering [47]. Part of fine granules of the RTP powder escapes from the gap between punches and die wall during the initial powder compaction and produces a ring surrounding the punches. This results in a change of the current pathways and formation of a hot spot in the centre of the pellet. Understanding the reason behind such peculiar densification inhomogeneity in samples and the temperature distribution, however, requires more studies. Nonetheless, the results obtained in this study indicate the pellets' centre might have experienced a significantly higher temperature during sintering, resulting in transparent centres of sintered pellets; the effects and results of *hot-zone* formation during SPS will be discussed further later on.

Although highly dense bodies were produced by spark plasma sintering, small pores remain at the grain boundaries. Pores' diameter is smaller than 100 nm ; although such pores have limited scattering effect at higher wavelengths ($> 1000\text{ nm}$), their effect becomes prominent in the ultraviolet region of the spectrum ($< 400\text{ nm}$) where the light wavelength is comparable with the effective diameter of the residual pore.

4.2. Carbon contamination

Carbon contamination becomes significant and is responsible for the light transmission decrease in samples fabricated using $T_c > 1150\text{ }^{\circ}\text{C}$. Although graphite particles can be introduced directly to the ceramic bodies produced by SPS, [23] Raman analyses revealed highly disordered or glassy carbon in the samples, which is entirely different from possible carbon contamination source (graphite paper). This rules out direct contamination by debris from graphite paper. Moreover, all samples were subjected to the same cooling process and, thus, the carbon contamination is unlikely to occur during cooling.

Kim et al. reported that annealing spinel powder prior to spark plasma sintering removes volatile species and results in higher transparency, and concluded that carbon-containing species present a priori in powder cause carbon contamination during SPS [48]. In other works, the graphite die/paper is shown to be responsible for carbon contamination [30,31]. In our case, the presence of some carbonate species was confirmed by Raman analysis (see Fig. 5); it is, therefore, important to verify the source of carbon contamination. The formation of solid carbon in pores from volatile species can be expressed by Boudouard's reaction:

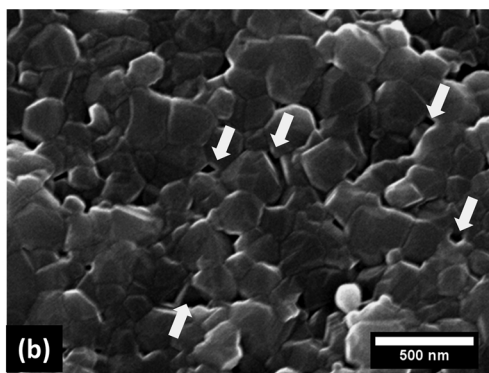
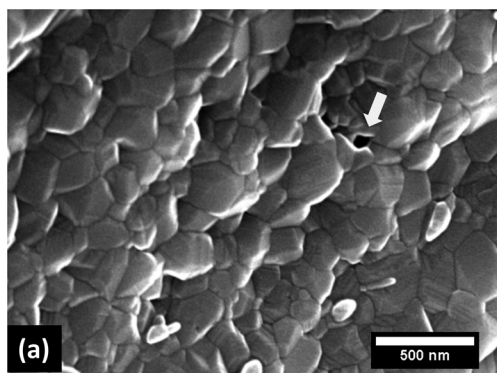


Fig. 9. Scanning electron microscopy images of the fracture surface of samples SPSed at $1250\text{ }^{\circ}\text{C}$ with $T_c = 1100\text{ }^{\circ}\text{C}$; the images were taken from (a) the centre of sample and (b) close to the edge of the sample. The samples were subjected to a heat treatment at $1150\text{ }^{\circ}\text{C}$ for 30 min to remove the residual carbon from the pores. Arrows indicate trapped pores.

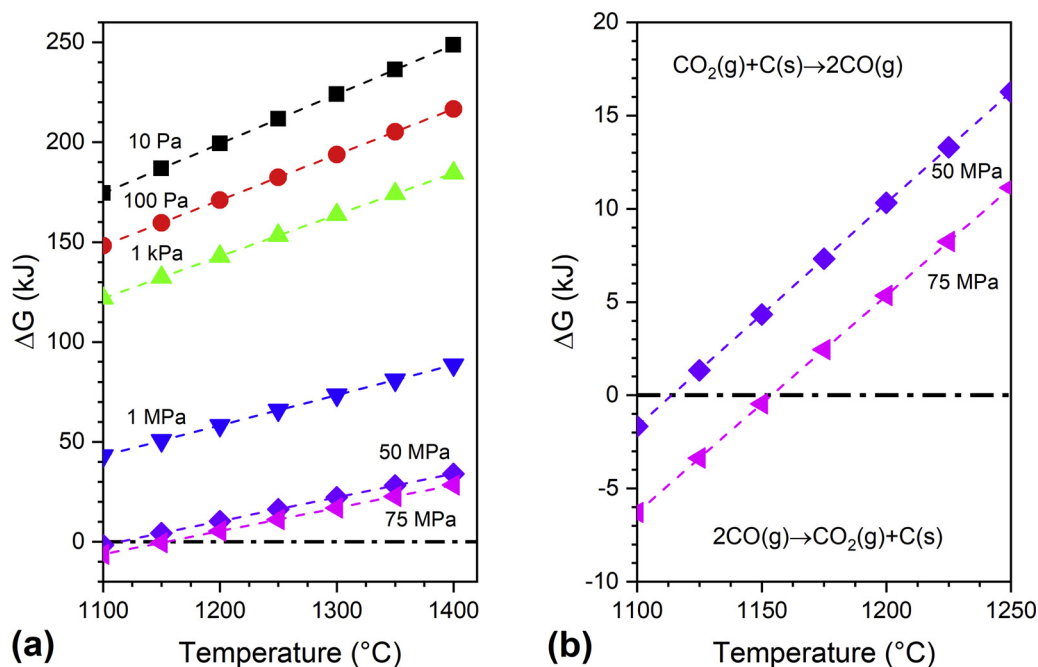


Fig. 10. Changes of the Gibbs free energy as a function of temperature for the formation of solid carbon from the reaction of oxides trapped in the closed pores under hydrostatic pressures between 10 Pa to 75 MPa (equal to the applied pressure during SPS process). Gibbs free energy vs. temperature: (a) 1100–1400 °C-P=10 Pa- 75 MPa, (b) 1100–1250 °C-P = 50 MPa and 75 MPa.

The Gibbs free energy variations of Boudouard's reaction against temperature change was calculated using FactSage® software by assuming most stable carbon phases are produced and considering the total pressure inside closed pores varying between 10 Pa (vacuum applied in the SPS chamber) and 75 MPa (the nominal applied mechanical pressure during SPS). Immediately after the closure of pores, the pressure of gasses trapped in them is assumed to be equal to the vacuum pressure in the SPS chamber. As the pores shrink by sintering, the pressure increases, until it reaches the maximum value of 75 MPa, i.e. the hydrostatic pressure in the pores equilibrates with the applied external mechanical pressure. Fig. 10 shows the variation of Gibbs free energy for Eq. 2 as a function of temperature; the temperature windows between 1100 °C and 1250 °C is enlarged in Fig. 10b. Under low pressures Gibbs' free energy of Eq. 2 is positive indicating carbon deposition is not thermodynamically favoured. The negative free energy of reaction below 1150 °C in Fig. 10b, implies that the deposition of carbon from volatile species occurs only at low temperatures under high pressures. In contrast, samples produced using T_c of 1100 and 1150 °C, which are exposed to the carbon deposition conditions for a longer time, show higher transparency compared to those produced using $T_c = 1175$ °C and 1200 °C. Thus, carbonate species are unlikely to be the cause of carbon contamination.

It is also interesting to investigate how carbon contamination is distributed in the samples; Raman spectra were collected in two directions: along the radii of the pellets, and across the thickness in the centre of the pellets. The spectrum collected in each point was treated by removing the background and fitting carbon's D, G and D' peaks using a Gaussian function following least-squares curve fitting approach [49]. The amplitude of the peaks was used to evaluate the concentration of respective species. Fig. 11 shows the distribution of carbon and the ratio of carbon D-band to G-band in the samples produced using the critical temperature of 1175 °C. Carbon contamination is distributed almost uniformly across the height of samples (Fig. 11a), with 3 times higher concentration of disordered carbon (D-Band) than highly ordered carbon (G-band). On the contrary, carbon contamination is concentrated in the centre of the sample followed by a gradual decrease towards the edges (Fig. 11b). The disordered carbon (D-Band) distribution resembles typical error function from the centre to the edge (dashed line in the graph). The contamination of samples due to carbon diffusion from the carbon paper should produce a concentration

gradient decreasing from the edge towards the centre of plots; this is opposite to the measured concentration profiles. Therefore, carbon distribution seems to be a result of the temperature gradient in the samples. Moreover, the uniaxial distribution of carbon suggests that it is introduced into samples through a deposition process from the atmosphere with increased partial pressure of carbon in the furnace. According to Morita et al., carbon contamination during SPS of MgAl_2O_4 occurs as a result of reactions between graphite die/paper and magnesium aluminate spinel powder, especially when high heating rates are applied [29–31]. Wang et al. reported on the fabrication of transparent magnesium aluminate spinel ceramics using two-step pressure profile [28]. The sintering programme consisted of an initial low-pressure step followed by the application of high pressure in the final step; the results showed that applying a lower pressure for a shorter time results in lower carbon contamination during spark plasma sintering.

Magnesium aluminate might react with carbon resulting in the deposition of glassy carbon in samples; therefore, it is worth investigating further the impact of applied pressure on carbon contamination. The reaction of magnesium aluminate spinel with the carbon impurity present in the pores, which is coming from graphite die/paper, can be simplified and written as [49] :



Fig. 12 shows the variation of Gibbs' free energy of Eq. 3 as a function of the temperature under different pressures between the pressure corresponding to the vacuum (10 Pa) and pressure related to the pressure applied by punches (75 MPa), which is considered to be equal to the equilibrium pressure of gasses trapped in closed pores. The Gibbs' free energy decreases continuously with the temperature; however, in the whole relevant temperature interval, the free energy has always a positive value.

The free energy of the reaction is negative above 1300 °C and only under the reaction pressure below 50 Pa. The formation of gases and the magnesium aluminate spinel degradation is therefore energetically favoured at temperatures below 1300 °C under vacuum (10 Pa). The positive reaction free energy at the higher pressures, i.e. above 50 Pa, implies that solid phases, carbon, MgAl_2O_4 , and possibly other oxides such as MgO and Al_2O_3 , are stable.

Taking into account the changes of the stability of phases upon the application of pressure, the following mechanism can be proposed for

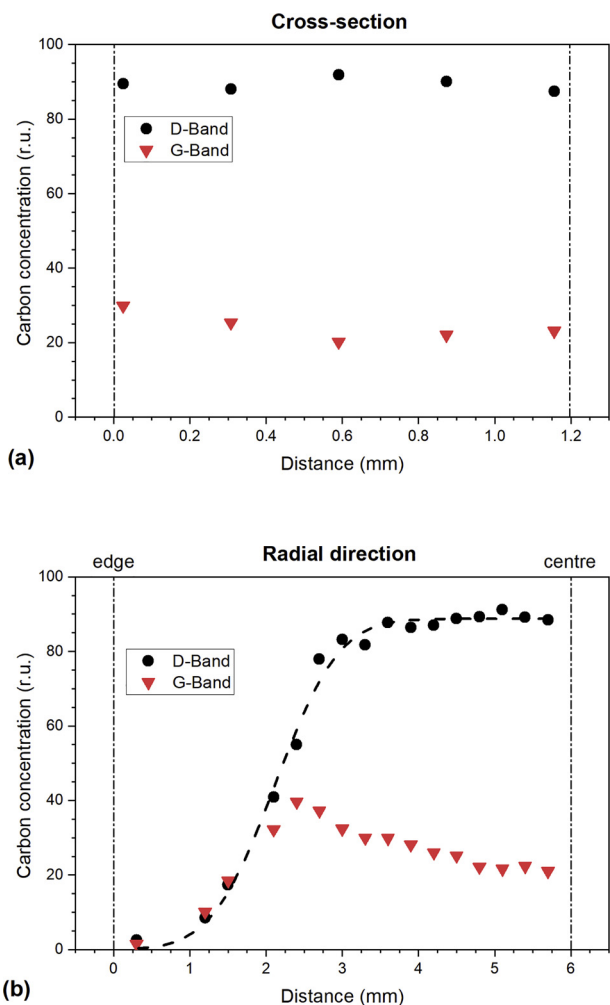


Fig. 11. Carbon concentration profile over polished cross-section of samples SPSed at 1250 °C using $T_c = 1175$ °C. The intensities of carbon D-band and G-bands, in relative units (r.u.), are shown to represent the concentration of carbon over: (a) the sample thickness at the centre and (b) along the radial axis of the disks.

the generation of carbon contamination in the transparent spinel bodies produced during the two-stage spark plasma sintering.

During the initial stages of sintering, the pores are connected, and, therefore, the gas pressure is equal to the vacuum applied during SPS. The fast heating in the first stage of sintering programme (100 °C min^{-1}) and the changes in electrical pathways result in the formation of hot zones close to the pellet’s centre. Consequently, the local temperature could exceed the critical temperature of magnesium aluminate degradation resulting in the formation of carbon-containing gases. Further densification produces closed pores, in which the hydrostatic pressure of entrapped gasses increases, eventually equilibrating the mechanical pressure applied the punches. The increase of pressure and the formation of hot zones provides the thermodynamically favourable conditions for the deposition of carbon and MgAl_2O_4 . The local temperature and size of hot zones increases when a higher critical temperature is applied (i.e. 1100 vs 1200 °C), which is reflected in the formation of larger black areas of samples produced at $T_c = 1200$ °C.

5. Summary and conclusions

Transparent magnesium aluminate spinel was fabricated using two-stage spark plasma sintering of a commercial MgAl_2O_4 powder: a high heating rate, 100 °C min^{-1} , was used up to a T_c , critical temperature, between 1100 and 1200 °C. Subsequently, the heating rate was slowed down to 2.5 °C min^{-1} , until the maximum temperature of 1250 °C was reached. Transparent bodies are obtained at a critical temperature lower than 1150 °C. Discolouration and lack of transparency observed in the samples sintered at the applied $T_c > 1150$ °C was caused by carbon contamination.

The critical temperature has a decisive role in achieving transparency. Samples produced using a critical temperature lower than 1150 °C exhibit a higher in-line transmission compared to those prepared using a higher critical temperature. The level of carbon contamination decreases with decreasing critical temperature. Visual inspection and analysis of Raman spectra confirmed that carbon contamination is distributed inhomogeneously. The formation of hot zones in the centre of sintered compacts is responsible for inhomogeneous densification. Thermodynamic calculations indicate that local increase of temperature can cause reactions between spinel and graphite paper/die, producing volatile gasses. Increase of pressure in closed pores changes the thermodynamics conditions favouring the formation of disordered carbon

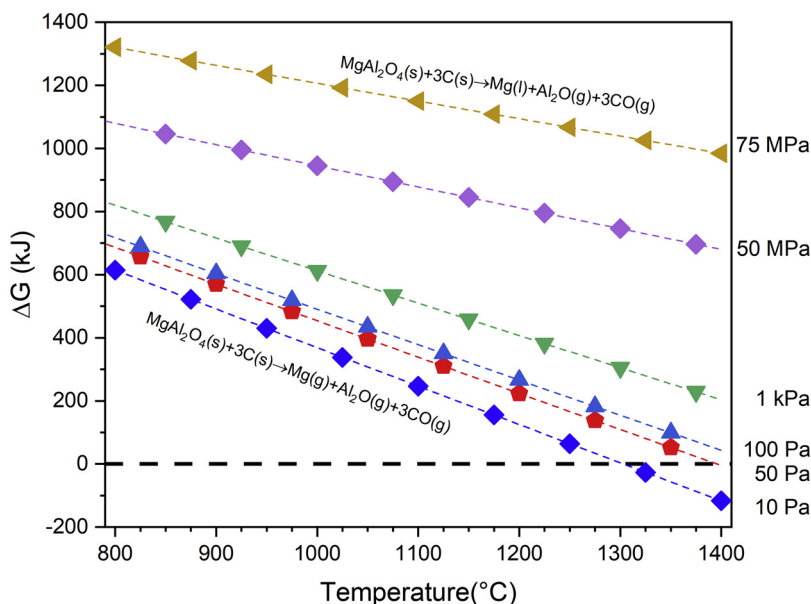


Fig. 12. Comparison of the Gibbs free energy change for the reaction of MgAl_2O_4 with graphite and formation of gasses according to Eq. 4 under vacuum (10 Pa) and a hydrostatic pressure applied during the SPS (75 MPa). The dashed line points out $\Delta G = 0$.

precipitates, which act as light scattering centres.

Declaration of Competing Interest

The authors declare that they have no known competing financial interests or personal relationships that could have appeared to influence the work reported in this paper.

Acknowledgement

This paper is a part of dissemination activities of the project FunGlass. This project has received funding from the European Union's Horizon 2020 research and innovation programme under grant agreement No 739566. Financial support of this work by the grants SAS-MOST JRP 2015/6, and VEGA 2/0026/17 is gratefully acknowledged. We appreciate the support provided by the Czech Ministry of Education under grant LTT18013 Inter-Transfer.

We appreciate helpful discussions and useful comments of Dr K. Griebenow on Raman Analyses of samples. We also appreciate the help of Prof M. Liska and Prof R. Klement with thermodynamic calculations and optical measurements.

References

- [1] K. Izumi, S. Miyazaki, S. Yoshida, T. Mizokawa, E. Hanamura, Optical properties of 3d transition-metal-doped MgAl₂O₄ spinels, *Physical Review B* 76 (7) (2007).
- [2] M. Rubat du Merac, H.-J. Kleebe, M.M. Müller, I.E. Reimanis, Fifty years of research and development coming to fruition; unraveling the complex interactions during processing of transparent magnesium aluminate (MgAl₂O₄) spinel, *J. Am. Ceram. Soc.* 96 (11) (2013) 3341–3365.
- [3] S.F. Wang, J. Zhang, D.W. Luo, F. Gu, D.Y. Tang, Z.L. Dong, G.E.B. Tan, W.X. Que, T.S. Zhang, S. Li, L.B. Kong, Transparent ceramics: processing, materials and applications, *Prog. Solid State Chem.* 41 (1–2) (2013) 20–54.
- [4] A. Goldstein, Correlation between MgAl₂O₄-spinel structure, processing factors and functional properties of transparent parts (progress review), *J. Eur. Ceram. Soc.* 32 (11) (2012) 2869–2886.
- [5] K.E. Sickafus, J.M. Wills, N.W. Grimes, Structure of spinel, *J. Am. Ceram. Soc.* 82 (12) (2004) 3279–3292.
- [6] L. Esposito, A. Piancastelli, S. Martelli, Production and characterization of transparent MgAl₂O₄ prepared by hot pressing, *J. Eur. Ceram. Soc.* 33 (4) (2013) 737–747.
- [7] K. Morita, B.-N. Kim, H. Yoshida, K. Hiraga, Densification behavior of a fine-grained MgAl₂O₄ spinel during spark plasma sintering (SPS), *Scripta Mater.* 63 (6) (2010) 565–568.
- [8] M. Sokol, M. Halabi, S. Kalabukhov, N. Frage, Nano-structured MgAl₂O₄ spinel consolidated by high pressure spark plasma sintering (HPSPS), *J. Eur. Ceram. Soc.* 37 (2) (2017) 755–762.
- [9] S.M. Hosseini, Structural, electronic and optical properties of spinel MgAl₂O₄ oxide, *Phys. Status Solidi B* 245 (12) (2008) 2800–2807.
- [10] G. Gilde, P. Patel, P. Patterson, D. Blodgett, D. Duncan, D. Hahn, Evaluation of hot pressing and hot isostatic pressing parameters on the optical properties of spinel, *J. Am. Ceram. Soc.* 88 (10) (2005) 2747–2751.
- [11] J.M. Kim, H.N. Kim, Y.J. Park, J.W. Ko, J.W. Lee, H.D. Kim, Fabrication of transparent MgAl₂O₄ spinel through homogenous green compaction by microfluidization and slip casting, *Ceram. Int.* 41 (10) (2015) 13354–13360.
- [12] C. Gajdowski, J. Bohmler, Y. Lorgouiloux, S. Lemonnier, S. d'Astorg, E. Barraud, A. Leriche, Influence of post-HIP temperature on microstructural and optical properties of pure MgAl₂O₄ spinel: from opaque to transparent ceramics, *J. Eur. Ceram. Soc.* 37 (16) (2017) 5347–5351.
- [13] I. Ganesh, G.J. Reddy, G. Sundararajan, S.M. Olhero, P.M.C. Torres, J.M.F. Ferreira, Influence of processing route on microstructure and mechanical properties of MgAl₂O₄ spinel, *Ceram. Int.* 36 (2) (2010) 473–482.
- [14] S. Bhaduri, S.B. Bhaduri, Microstructural and mechanical properties of nanocrystalline spinel and related composites, *Ceram. Int.* 28 (2) (2002) 153–158.
- [15] C. Aksel, B. Rand, F.L. Riley, P.D. Warren, Mechanical properties of magnesia-spinel composites, *J. Eur. Ceram. Soc.* 22 (5) (2002) 745–754.
- [16] G. Bonnefont, G. Fantozzi, S. Trombert, L. Bonneau, Fine-grained transparent MgAl₂O₄ spinel obtained by spark plasma sintering of commercially available nanopowders, *Ceram. Int.* 38 (1) (2012) 131–140.
- [17] N. Frage, S. Cohen, S. Meir, S. Kalabukhov, M.P. Dariel, Spark plasma sintering (SPS) of transparent magnesium-aluminate spinel, *J. Mater. Sci.* 42 (9) (2007) 3273–3275.
- [18] M. Sokol, S. Kalabukhov, M.P. Dariel, N. Frage, High-pressure spark plasma sintering (SPS) of transparent polycrystalline magnesium aluminate spinel (PMAS), *J. Eur. Ceram. Soc.* 34 (16) (2014) 4305–4310.
- [19] S. Cohen, B. Ratzker, M. Sokol, S. Kalabukhov, N. Frage, Polycrystalline transparent magnesium aluminate spinel processed by a combination of spark plasma sintering (SPS) and hot isostatic pressing (HIP), *J. Eur. Ceram. Soc.* 38 (15) (2018) 5153–5159.
- [20] K. Morita, B.N. Kim, K. Hiraga, H. Yoshida, Fabrication of transparent MgAl₂O₄ spinel polycrystal by spark plasma sintering processing, *Scripta Mater.* 58 (12) (2008) 1114–1117.
- [21] M.M. Muller, H.J. Kleebe, Sintering mechanisms of LiF-Doped Mg-Al-Spinel, *J. Am. Ceram. Soc.* 95 (10) (2012) 3022–3024.
- [22] L. Ramond, G. Bernard-Granger, A. Addad, C. Guizard, T. Rouxel, Sintering of soda-lime glass microspheres using spark plasma sintering, *J. Am. Ceram. Soc.* 94 (9) (2011) 2926–2932.
- [23] A. Bertrand, J. Carreaud, G. Delaizir, J.R. Duclere, M. Colas, J. Cornette, M. Vandenhende, V. Couderc, P. Thomas, A comprehensive study of the carbon contamination in tellurite glasses and glass-ceramics sintered by spark plasma sintering (SPS), *J. Am. Ceram. Soc.* 97 (1) (2014) 163–172.
- [24] K. Rozenburg, I.E. Reimanis, H.J. Kleebe, R.L. Cook, Sintering kinetics of a MgAl₂O₄ spinel doped with LiF, *J. Am. Ceram. Soc.* 91 (2) (2008) 444–450.
- [25] I.E. Reimanis, H.J. Kleebe, Reactions in the sintering of MgAl₂O₄ spinel doped with LiF, *Int. J. Mater. Res.* 98 (12) (2007) 1273–1278.
- [26] A. Goldstein, J. Raethel, M. Katz, M. Berlin, E. Galun, Transparent MgAl₂O₄/LiF ceramics by hot-pressing: host-additive interaction mechanisms issue revisited, *J. Eur. Ceram. Soc.* 36 (7) (2016) 1731–1742.
- [27] G.R. Villalobos, J.S. Sanghera, I.D. Aggarwal, Degradation of magnesium aluminum spinel by lithium fluoride sintering aid, *J. Am. Ceram. Soc.* 88 (5) (2005) 1321–1322.
- [28] C. Wang, Z. Zhao, Transparent MgAl₂O₄ ceramic produced by spark plasma sintering, *Scripta Mater.* 61 (2) (2009) 193–196.
- [29] K. Morita, B.N. Kim, H. Yoshida, K. Hiraga, Y. Sakka, Influence of spark plasma sintering (SPS) conditions on transmission of MgAl₂O₄ spinel, *J. Am. Ceram. Soc.* 98 (2) (2015) 378–385.
- [30] K. Morita, B.-N. Kim, H. Yoshida, K. Hiraga, Y. Sakka, Distribution of carbon contamination in MgAl₂O₄ spinel occurring during spark-plasma-sintering (SPS) processing: I – effect of heating rate and post-annealing, *J. Eur. Ceram. Soc.* 38 (6) (2018) 2588–2595.
- [31] K. Morita, B.N. Kim, H. Yoshida, K. Hiraga, Y. Sakka, Distribution of carbon contamination in oxide ceramics occurring during spark-plasma-sintering (SPS) processing: II - Effect of SPS and loading temperatures, *J. Eur. Ceram. Soc.* 38 (6) (2018) 2596–2604.
- [32] L.M. Fraas, J.E. Moore, J.B. Salzberg, Raman characterization studies of synthetic and natural MgAl₂O₄ crystals, *J. Chem. Phys.* 58 (9) (1973) 3585–3592.
- [33] M.P. O'Horo, A.L. Frisillo, W.B. White, Lattice vibrations of MgAl₂O₄ spinel, *J. Phys. Chem. Solids* 34 (1) (1973) 23–28.
- [34] R. Caracas, E.J. Banigan, Elasticity and Raman and infrared spectra of MgAl₂O₄ spinel from density functional perturbation theory, *Phys. Earth Planet. Inter.* 174 (1–4) (2009) 113–121.
- [35] M. Lazzari, P. Thibaudeau, Ab initio Raman spectrum of the normal and disordered MgAl₂O₄ spinel, *Phys. Rev. B* 74 (14) (2006).
- [36] S. Gunasekaran, G. Anbalagan, S. Pandi, Raman and infrared spectra of carbonates of calcite structure, *J. Raman Spectrosc.* 37 (9) (2006) 892–899.
- [37] M.I. Burrueco, M. Mora, J.-S.-C. Of Molecular ..., Raman microspectroscopy of hydroxalcalite-like compounds modified with sulphate and sulphate organic anions, *Journal of Molecular* (2013).
- [38] N. Benameur, G. Bernard-Granger, A. Addad, S. Raffy, C. Guizard, Sintering analysis of a fine-grained alumina-magnesia spinel powder, *J. Am. Ceram. Soc.* 94 (5) (2011) 1388–1396.
- [39] A. Talimian, V. Pouchly, H.F. El-Maghraby, K. Maca, D. Galusek, Impact of high energy ball milling on densification behaviour of magnesium aluminate spinel evaluated by master sintering curve and constant rate of heating approach, *Ceram. Int.* 45 (17, Part B) (2019) 23467–23474.
- [40] G. Bernard-Granger, N. Benameur, A. Addad, M. Nygren, C. Guizard, S. Deville, Phenomenological analysis of densification mechanism during spark plasma sintering of MgAl₂O₄, *J. Mater. Res.* 24 (6) (2011) 2011–2020.
- [41] B. Ratzker, M. Sokol, S. Kalabukhov, N. Frage, Creep of polycrystalline magnesium aluminate spinel studied by an SPS apparatus, *Materials Basel* (Basel) 9 (6) (2016) 493.
- [42] H. Palmour, D.M. Choi, L.D. Barnes, R.D. McBrayer, W.W. Krieger, Deformation in hot-pressed polycrystalline spinel, in: H.H. Stadelmaier, W.W. Austin (Eds.), *Materials Science Research*, Springer US, Boston, MA, 1963, pp. 158–197.
- [43] J.-H. Lee, B.-N. Kim, B.-K. Jang, Non-uniform sintering behavior during spark plasma sintering of Y₂O₃, *Ceram. Int.* 46 (3) (2020) 4030–4034.
- [44] B. Ratzker, A. Wagner, M. Sokol, S. Kalabukhov, M.P. Dariel, N. Frage, Optical and mechanical properties of transparent alumina fabricated by high-pressure spark plasma sintering, *J. Eur. Ceram. Soc.* 39 (8) (2019) 2712–2719.
- [45] P. Mondalek, L. Silva, M. Bellet, A numerical model for powder densification by SPS technique, *Adv. Eng. Mater.* 13 (7) (2011) 587–593.
- [46] J. Rathel, M. Herrmann, W. Beckert, Temperature distribution for electrically conductive and non-conductive materials during Field Assisted Sintering (FAST), *J. Eur. Ceram. Soc.* 29 (8) (2009) 1419–1425.
- [47] P.S. Colasuonno, Method for Creating Functionally Graded Materials With Spark Plasma Sintering and a Continuous Machine for Future Scalability, Colorado State University, 2017.
- [48] B.N. Kim, K. Morita, J.H. Lim, K. Hiraga, H. Yoshida, Effects of preheating of powder before spark plasma sintering of transparent MgAl₂O₄ spinel, *J. Am. Ceram. Soc.* 93 (8) (2010) 2158–2160.
- [49] A.C. Ferrari, J. Robertson, Interpretation of Raman spectra of disordered and amorphous carbon, *Phys. Rev. B* 61 (20) (2000) 14095–14107.